Photoneutron cross sections for samarium isotopes: Toward a unified understanding of (γ,n) and (n,γ) reactions in the rare earth region

D. M. Filipescu,[1,2] I. Gheorghe,[1,2,3] H. Utsunomiya,[4,5] S. Goriely,[6] T. Renstrøm,[7] H.-T. Nyhus,[7] O. Tesileanu,[1] T. Glodariu,[2] T. Shima,[8] K. Takahisa,[8] S. Miyamoto,[9] Y.-W. Lui,[10] S. Hilaire,[11] S. Péru,[11] M. Martini,[6,11,12] and A. J. Koning[13]

[1]*Extreme Light Infrastructure Nuclear Physics, 407 Atomistilor Str., P.O. Box MG6, Bucharest-Magurele, Romania*

[2]*National Institute for Physics and Nuclear Engineering Horia Hulubei, 407 Atomistilor Str., P.O. Box MG6, Bucharest-Magurele, Romania*

[3]*Faculty of Physics, University of Bucharest, RO-077125, Bucharest, Romania*

[4]*Department of Physics, Konan University, Okamoto 8-9-1, Higashinada, Kobe 658-8501, Japan*

[5]*Center for Nuclear Study, University of Tokyo, 2-1 Hirosawa, Wako, Saitama 351-0198, Japan*

[6]*Institut d'Astronomie et d'Astrophysique, Université Libre de Bruxelles, Campus de la Plaine, CP-226, 1050 Brussels, Belgium*

[7]*Department of Physics, University of Oslo, N-0316 Oslo, Norway*

[8]*Research Center for Nuclear Physics, Osaka University, Suita, Osaka 567-0047, Japan*

[9]*Laboratory of Advanced Science and Technology for Industry, University of Hyogo, 3-1-2 Kouto, Kamigori, Ako-gun, Hyogo 678-1205, Japan*

[10]*Cyclotron Institute, Texas A&M University, College Station, Texas 77843, USA*

[11]*CEA, DAM, DIF, F-91297 Arpajon, France*

[12]*Department of Physics and Astronomy, Ghent University, Proeftuinstraat 86, B-9000 Gent, Belgium*

[13]*Nuclear Research and Consultancy Group, P.O. Box 25, NL-1755 ZG Petten, The Netherlands*

(Received 6 October 2014; revised manuscript received 24 November 2014; published 22 December 2014)

Photoneutron cross sections were measured for the seven stable samarium isotopes ^{144,147,148,149,150,152,154}Sm near the neutron threshold with quasi-monochromatic laser-Compton scattering γ rays. Our photoneutron cross sections are found to be low by 20%–37% relative to existing data. The photoneutron data are analyzed with the TALYS reaction code by considering the Skyrme Hartree-Fock-Bogoliubov (HFB) plus quasiparticle random phase approximation (QRPA) model and the axially symmetric deformed Gogny HFB plus QRPA model of the $E1$ γ-ray strength. Using the γ-ray strength function constrained by the present photoneutron data, we made a thorough analysis of the reverse (n,γ) cross sections including the radioactive nucleus ^{151}Sm with a half-life of 90 yr. The radiative neutron capture cross section for ^{153}Sm with the half-life of 1.928 d is deduced with the γ-ray strength function method.

DOI: 10.1103/PhysRevC.90.064616 PACS number(s): 25.20.Lj, 25.40.Lw, 27.60.+j, 26.20.Kn

I. INTRODUCTION

Radiative neutron capture on radioactive nuclei along the line of β stability in the medium- to heavy-mass region of the chart of nuclei is an important issue in nuclear astrophysics and nuclear engineering. In nuclear astrophysics, the cross sections are important to determine the s-process path at branching points where neutron capture and β decay compete [1]. The neutron capture data are also essential for nuclear transmutation of long-lived fission products known as nuclear waste in the field of nuclear engineering [2]. The γ-ray strength function (γSF) method was recently devised for constraining the (n,γ) cross section of radioactive nuclei, which cannot be measured directly [3,4]. This method relies on the Brink hypothesis linking photodeexcitation to photoabsorption [5] and aims at determining the γSF, a nuclear statistical quantity that is commonly important to quantify radiative neutron capture and photoneutron cross sections. Photoneutron cross sections provide a stringent experimental constraint in absolute scale on the γSF around the neutron emission threshold S_n. The method requires a systematic measurement of photoneutron cross sections for neighboring stable isotopes of a radioactive nucleus of interest, in addition to the existing (n,γ) data which serve as experimental constraints on the γSF below S_n. Thus, a unified understanding of (n,γ) and (γ,n) cross sections throughout an isotopic chain offers detailed information on the γSF for a given nucleus formed by neutron capture on the radioactive nucleus. Such a systematic approach with the γSF method has been applied to zirconium [6], tin [7], molybdenum [8], and neodymium [9] isotopes.

We now apply the γSF method to the Sm isotopic chain. The γSF method requires a systematic measurement of photoneutron cross sections for stable Sm isotopes in the vicinity of the radioactive Sm isotopes. Figure 1 illustrates the photoneutron emission and radiative neutron capture of Sm isotopes studied in the present paper. The present photoneutron measurement involved seven stable isotopes including the p-process nucleus ^{144}Sm, the s-only nuclei ^{148}Sm and ^{150}Sm, and the r-only nucleus ^{154}Sm as shown by the left-pointing arrows in Fig. 1. The photoneutron emissions studied constitute a part of the reaction network of the p-process nucleosynthesis [10] in which photodisintegration plays a primary role in reprocessing the preexisting nuclei produced by the s-process and r-process [11]. Photoneutron cross sections for two odd-N nuclei, ^{147}Sm and ^{149}Sm, are measured for the first time. The ^{147}Sm(γ,n) reaction is important for the production of the p-process ^{146}Sm chronometer [10]. The photodisintegration of ^{144}Sm also contributes to the destruction of this p-process nucleus.

We present radiative neutron capture cross sections for ^{153}Sm (half-life of 1.928 d) and ^{151}Sm (half-life of 90 yr) determined with the γSF method. The latter cross section

 ©2014 American Physical Society

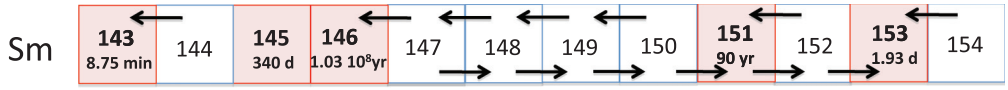

FIG. 1. (Color online) The chart of nuclei depicting our systematic analysis of (γ,n) and (n,γ) cross sections for Sm isotopes in the context of the γ-ray strength function method. Photoneutron cross sections measured in the present experiment are shown by left-pointing arrows. Radiative neutron capture cross sections discussed in the present systematic analysis are shown by right-pointing arrows. The radiative neutron capture cross section of the radioactive nucleus ^{153}Sm is deduced with the γ-ray strength function method.

is compared with the direct measurement carried out at the CERN-nTOF facility [12,13].

The outline of the paper is given as follows: The experimental procedure is described in Sec. II, while details regarding the data analysis are given in Sec. III. The theoretical analysis for the photoneutron emission is described in Sec. IV. The radiative neutron capture cross sections, together with the determination of the ^{153}Sm$(n,\gamma)^{154}$Sm cross section through the γSF method, are analyzed in Sec. V . Finally, conclusions are drawn in Sec. VI.

II. EXPERIMENTAL PROCEDURE

Photoneutron cross section measurements for the stable isotopes of samarium have been performed by using γ-ray beams produced by the Compton backscattering of laser photons on relativistic electrons (LCS γ rays) at the NewSUBARU synchrotron radiation facility [14]. We present here details about γ beam production, beam energy profile, target preparation, neutron detection, and beam flux monitoring.

A. Gamma production and energy profile measurements

LCS γ-ray beams were produced with a high power Q-switch Nd : YVO_4 laser INAZUMA (Spectra-Physics) and electron beams at energies between 573 and 850 MeV. The maximum energy of the LCS γ-ray beams was varied from the corresponding neutron emission threshold (S_n) of each Sm isotope (the lowest value of which is 5.87 MeV for ^{149}Sm) to 13 MeV, in the fundamental mode of the laser operation ($\lambda = 1064$ nm; power = 40 W). The laser was operated at a 20-kHz frequency and had a pulsed, 10-Hz macroscopic time structure of 80 ms beam-on and 20 ms beam-off. The electron beam intensity varied from 200 to 65 mA, decreasing by approximately 12–13 mA per hour.

The γ-ray beamline of the NewSUBARU synchrotron radiation facility is depicted in Fig. 2. The laser beam was focused in the vicinity of the midpoint (P2) of the straight section of the ring used for laser-electron interactions, where the electron beam has a minimum transverse profile and the probability of LCS interactions becomes maximum [14]. The LCS γ-ray beams were collimated with a 10-cm-thick lead block with a 2-mm opening (C2 collimator in Hutch 1) that is located 18.47 m from the interaction point. The collimator mounted on an x-y-θ stage driven by stepping motors was aligned to optimize the γ-ray flux by monitoring with a NaI(Tl) detector. The γ-ray beamline is equipped with a double collimation system with a 10-cm C1 lead collimator with 6- or 3-mm opening, which is located in the accelerator vault 3.00 m upstream from the C2 collimator. The experiment was carried out with and without the C1 collimator.

The γ-ray energy profile was measured with a large-volume 3.5″ × 4″ lanthanum bromide ($LaBr_3$: Ce) detector in Hutch 2, GACKO (Gamma Collaboration Hutch of Konan University). Hourly measurements were performed for each γ-ray beam energy with the laser operated in the continuous-wave mode at a reduced power in order to avoid pile-up effects.

The $LaBr_3$: Ce detector was calibrated by using the standard calibration sources ^{137}Cs and ^{60}Co including the 2.5-MeV sum peak of ^{60}Co, the 1436-keV peak resulting from the electron capture decay of ^{138}La, and the maximum energy of each LCS γ-ray beam produced in this experiment. The energy calibration of the $LaBr_3$: Ce detector is shown in Fig. 3. The calibration points were fitted with a second-order polynomial by using the χ^2 method. The energy resolution of the detector was studied by using γ transitions from the ^{137}Cs and ^{60}Co sources. An upper limit of 2% was obtained for energies above 2.5 MeV by fitting the data points with a $1/\sqrt{E}$ function, where E is the γ-ray energy.

The maximum energy of the LCS γ-ray beams is obtained by the known energy of the electrons and laser photons (1.164 eV). The electron beam energy was recently calibrated between 550 and 974 MeV in nominal energy with an accuracy of the order of 10^{-5} [15]. For this, a grating-fixed CO_2 laser ($\lambda = 10.5915$ μm) was used to produce low-energy LCS γ-ray beams below 1.7 MeV at the interaction point P1. The produced γ-ray beams were measured with a calibrated hyperpure Germanium (HPGe) detector. It was found that there

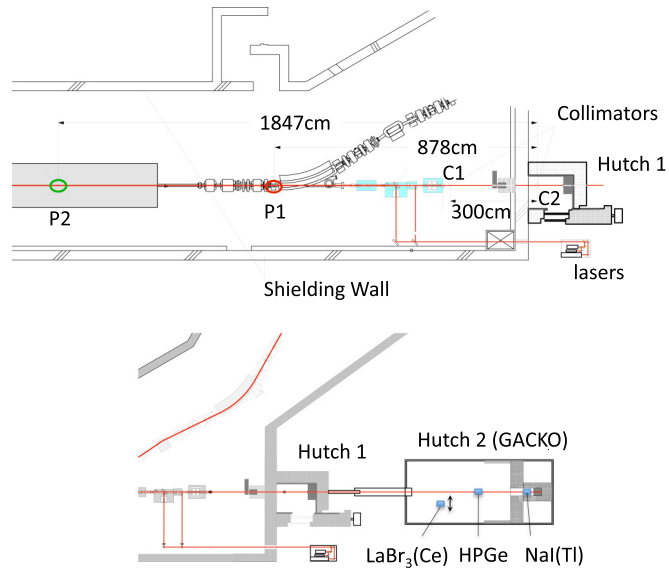

FIG. 2. (Color online) The γ-ray beamline at the NewSUBARU synchrotron radiation facility.

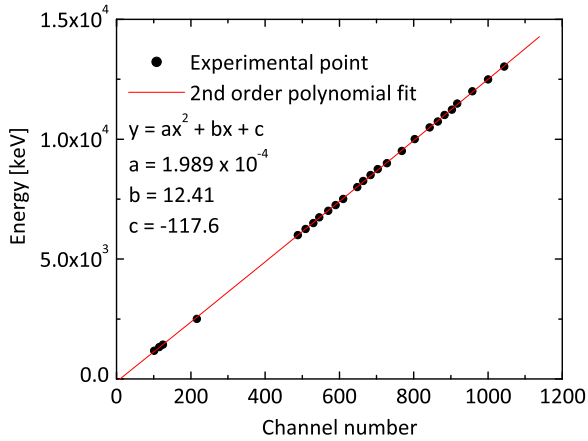

FIG. 3. (Color online) Energy calibration of the $LaBr_3$: Ce detector with ^{137}Cs, ^{60}Co, and ^{138}La and the maximum energies of LCS γ-ray beams produced using a Nd : YVO_4 laser and electron beams at energies between 573 and 850 MeV.

is a systematic difference of approximately 10 MeV between the nominal electron energy given by the beam optics of the storage ring and the calibrated energy.

The Compton backscattering of laser photons on relativistic electrons and the electromagnetic interactions of the γ-ray beams inside the $LaBr_3$: Ce detector were simulated by using the GEANT4 Monte Carlo code [16,17]. The kinematics of the inverse Compton scattering is implemented in the Monte Carlo code with inclusion of the effect of the electron beam emittance. The energy spectra of the LCS γ-ray beams incident on the targets were obtained by reproducing the $LaBr_3$: Ce detector response. A detailed description of the GEANT4 simulation is given in a separate paper [18].

Figure 4 shows a typical spectrum of the LCS γ-ray beam recorded with the $LaBr_3$: Ce detector (solid line) along with the GEANT4 simulations of the detector response

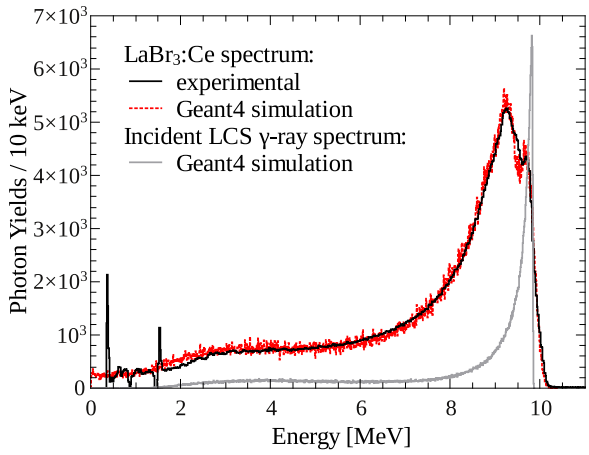

FIG. 4. (Color online) A typical spectrum of the γ-ray beam recorded with the $LaBr_3$: Ce detector (solid line) and the simulations of the response function (dotted line) and of the incident γ-ray beam (gray line). A single collimation with a C2 collimator of 2-mm aperture was used.

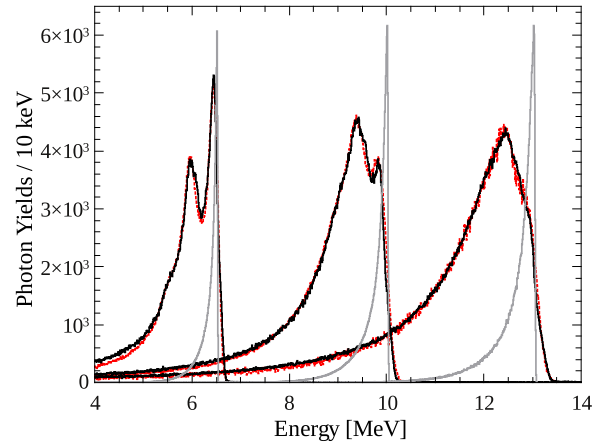

FIG. 5. (Color online) Typical spectra of the γ-ray beams recorded with the $LaBr_3$: Ce detector (solid lines) and the simulations of the response function (dotted lines) and of the incident γ-ray beam (gray lines). A double collimation with a C1 collimator of 6-mm aperture and a C2 collimator of 2-mm aperture was employed.

function (dotted line) and the incident γ-ray beam (gray line). The spectra are renormalized for better visualization. The experimental response function was obtained without the C1 collimator. One can see a broad low-energy bump around 3 MeV in the response function. This bump is characteristic of spectra obtained without the C1 collimator, which was confirmed experimentally under the presence and absence of the C1 collimator. The bump corresponds to the laser photons Compton-scattered around 0° with large cross sections in the rest frame of electrons which, after a Lorentz boost by relativistic electrons in the laboratory frame, punched through the 10-cm C2 collimator. The punch-through component is seen in the low-energy region of the incident γ-ray spectrum.

Figure 5 shows typical spectra of the LCS γ-ray beams recorded with the $LaBr_3$: Ce detector (solid lines) along with the GEANT4 simulations of the detector response function (dotted lines) and the incident γ-ray beam (gray lines). The experimental response functions were obtained by using the double collimation system with a C1 collimator of 6-mm aperture. The low-energy component is absent in the response function obtained with the double collimation system, which confines the scattering angles into a narrower cone along the electron beam axis with a total thickness of 20 cm. The experimental response functions are well reproduced by the GEANT4 simulation. Energy spreads of 1.2%, 1.4%, and 1.6% at full width at half maximum (FWHM) were obtained for the three incident γ-ray beams of maximum energy of 6.5, 10.0, and 13.0 MeV, respectively. Thus the $LaBr_3$: Ce detector is suitable for recording energy spectra of the γ-ray beams.

B. Target preparation

Enriched samples of ^{144}Sm, ^{147}Sm, ^{148}Sm, ^{149}Sm, ^{150}Sm, ^{152}Sm, and ^{154}Sm in oxide form (Sm_2O_3) placed in pure aluminum containers with inner diameter of 8 mm were irradiated by the γ-ray beams. The samples were dehydrated by baking in vacuum at temperatures up to 393°C for 4 h before

TABLE I. Enrichment and areal density of samples.

Sample	Purity (%)	Areal density (mg/cm^2)
^{144}Sm	88.80	1102
^{147}Sm	94.00	1042
^{148}Sm	99.94	2102
^{149}Sm	97.72	2242
^{150}Sm	94.68	862
^{152}Sm	99.47	1959
^{154}Sm	98.69	2253

being placed inside the aluminum containers. The sample masses were determined by weighing the containers before and after the filling. The γ-ray beam was positioned at the center of the target by monitoring the visible synchrotron radiation as a guide. According to the GEANT4 simulation, the beam spot on target is 2.3 mm in diameter, which is sufficiently smaller than the diameter of the target. The enrichment and the areal density of each sample are listed in Table I.

C. Neutron detection

The number of (γ,n) reactions was determined by detecting the reaction neutrons with a calibrated neutron detection array. The samarium samples were mounted at the center of a 4π neutron detector composed of 20 ^{3}He proportional counters embedded in a 36 $\times$ 36 $\times$ 50 cm^3 polyethylene moderator. The ^{3}He counters were placed in three concentric rings of four, eight, and eight proportional counters located 3.8, 7.0, and 10.0 cm from the beam axis, respectively. The moderator was surrounded by additional polyethylene plates with cadmium to suppress background neutrons. Every 100 ms of γ irradiation, reaction plus background neutrons were recorded for 80 ms of laser-on and background neutrons were recorded for 20 ms of laser-off. The average energy of the reaction neutrons was obtained using the "ring ratio technique" originally developed by Berman and Fultz [19] and used to determine the detection efficiency. More details of the neutron detection are found in the literature [20].

Neutron detection efficiencies of the three rings were measured after the present experiment by using a calibrated ^{252}Cf source with an emission rate of 2.27 $\times$ 10^4 s^{-1} with 2.2% uncertainty at the National Metrology Institute of Japan. The measurement excellently reproduced the results obtained in 2006 at the same institute, which can be seen in Ref. [20].

D. Beam flux monitoring

The γ-ray beam flux was monitored with a 6″ $\times$ 5″ NaI(Tl) detector placed at the end of the LCS γ-ray beam line. The Nd : YVO_4 (λ = 1.064 μm) laser operated at 20-kHz frequency produces pulses of light of 60 ns in duration. The electron beam bunches have a time structure of 2-ns interval (500 MHz) and 60-ps width. Thus, the LCS γ rays are generated in bunches corresponding to each laser light pulse. The number of LCS γ rays per bunch is given by a Poisson distribution [21] with a mean which depends on the laser and electron beam intensity, collimator aperture, and the probability of interaction between the laser photons and the relativistic electrons.

The number of recorded γ photons was obtained by using the "pile-up method" described in [21], which is based on the Poisson fitting method originally developed at the Electrotechnical Laboratory [22,23]. The uncertainty of the Poisson fitting method is estimated to be 3%, which is attributed to the fitting and the energy linearity of the γ-ray detector in its response to multiphotons. For each neutron measurement run we recorded the γ-ray spectra, when the laser is on in the full power mode. Multiple photons were detected simultaneously, generating a so-called pile-up spectrum. Before or after each neutron measurement run the laser power is reduced in order to obtain a single-photon spectrum, where it is most likely to measure only one photon at a time. A typical example of the experimental pile-up energy spectrum, along with the single-photon spectrum, is shown in Fig. 6.

The number of γ rays detected in the NaI detector, $N_{\gamma,\mathrm{det}}$, is given by

$$N_{\gamma,\mathrm{det}} = \frac{\langle i\rangle_{\mathrm{pileup}}}{\langle i\rangle_{\mathrm{single}}}\left(\sum n_i\right)_{\mathrm{pileup}}, \tag{1}$$

where $\langle i\rangle = (\sum x_i n_i)/(\sum n_i)$ gives the average channel of the pile-up and single-photon spectrum, and n_i is the number of counts in the ith channel. Note that the ratio of $\langle i\rangle$ in Eq. (1) gives the average number of γ photons involved in a γ-ray beam pulse, while the sum pile-up events give the number of γ-ray beam pulses. As the targets are quite thick, the attenuation of the γ rays in the target amounts to 2%–3%. Furthermore, to calculate the average γ-ray flux incident on the target we have to take into account the attenuation in the NaI detector as well,

$$N_\gamma = \frac{N_{\gamma,\mathrm{det}}}{\exp\left[-\frac{\mu_\mathrm{t}}{\rho_\mathrm{t}}t_\mathrm{t}\right]\left(1-\exp\left[-\frac{\mu_\mathrm{NaI}}{\rho_\mathrm{NaI}}t_\mathrm{NaI}\right]\right)}, \tag{2}$$

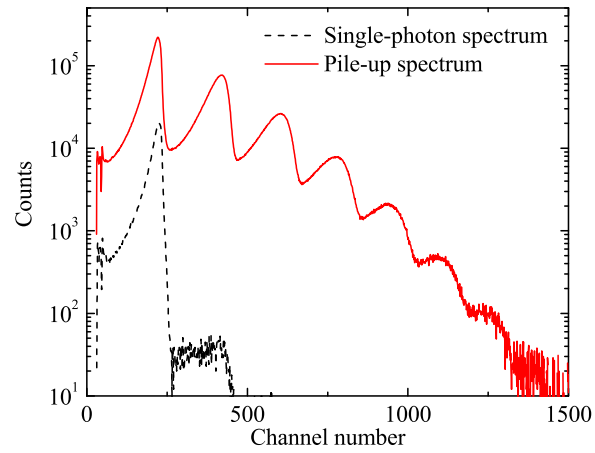

FIG. 6. (Color online) Experimental pile-up energy spectrum of the LCS γ-ray beam obtained with a 6″ $\times$ 5″ NaI(Tl) detector. A single-photon spectrum is also shown by the dashed line. The maximum energy of the LCS γ-ray beam is 13.03 MeV (electron beam energy of 860.8 MeV). The average number of photons per beam pulse is 1.78.

where t_t and t_{NaI} give the thickness (in g/cm^2) of the target and the NaI detector, respectively, and $\frac{\mu}{\rho}$ represents the mass attenuation coefficient (in cm^2/g), tabulated in Ref. [24].

The systematic uncertainty for the cross section breaks down to 3% for the number of incident photons, 3.2% for the neutron detection efficiency, 0.5%–0.7% for the number of target nuclei, and 0.2%–0.9% for the total attenuation coefficient. Thus, the overall systematic uncertainty amounts to 4.5% by summing the uncertainties of the breakdown in quadrature.

III. DATA REDUCTION

The photoneutron cross section is given by

$$\int_{S_n}^{E_{\mathrm{Max}}} n_\gamma(E_\gamma)\sigma_{\gamma n}(E_\gamma)dE_\gamma = \frac{N_n}{N_t N_\gamma \xi \epsilon_n g}, \quad (3)$$

where $n_\gamma(E_\gamma)$ gives the energy distribution of the γ-ray beam normalized to unity and $\sigma_{\gamma n}(E_\gamma)$ is the photoneutron cross section to be determined. Furthermore, N_n represents the number of neutrons detected, N_t gives the number of target nuclei per unit area, N_γ is the number of γ rays incident on target, ϵ_n represents the neutron detection efficiency, and finally $\xi = (1 - e^{\mu t})/(\mu t)$ gives a correction factor for a thick target measurement. The factor g represents the fraction of γ flux above the neutron threshold S_n,

$$g = \frac{\int_{S_n}^{E_{\mathrm{Max}}} n_\gamma(E_\gamma)dE_\gamma}{\int_0^{E_{\mathrm{Max}}} n_\gamma(E_\gamma)dE_\gamma}. \quad (4)$$

As a first approximation we assume a monochromatic γ-ray beam, by replacing the γ-energy distribution $n(E_\gamma)$ in Eq. (3) by a delta function, $\delta(E_\gamma - E_{\mathrm{av}})$. Here, E_{av} is the average energy of the LCS γ beam,

$$E_{\mathrm{av}} = \frac{\int_{S_n}^{E_{\mathrm{Max}}} E_\gamma n_\gamma(E_\gamma)dE_\gamma}{\int_{S_n}^{E_{\mathrm{Max}}} n_\gamma(E_\gamma)dE_\gamma}. \quad (5)$$

We obtain the following cross section in the monochromatic approximation:

$$\sigma_{\gamma n}^{\mathrm{mono}}(E_{\mathrm{av}}) = \frac{N_n}{N_t N_\gamma \xi \epsilon_n g}. \quad (6)$$

The next step is to take into account the measured energy distribution of the γ-ray beam. A Taylor expansion method [25] is used to solve the integral of Eq. (3) with respect to $\sigma_{\gamma n}(E_{\mathrm{av}})$ in the following manner:

$$\sigma_{\gamma n}(E_{\mathrm{av}}) + \sum_i s_i(E_{\mathrm{av}}) = \frac{N_n}{N_t N_\gamma \xi \epsilon_n g}, \quad (7)$$

where

$$s_i(E_{\mathrm{av}}) = \frac{1}{n!}\sigma_{\gamma n}^{(i)}(E_{\mathrm{av}}) \int_{S_n}^{E_{Max}} n_\gamma(E_\gamma)(E_\gamma - E_{\mathrm{av}})^i dE_\gamma, \quad (8)$$

and where $\sigma_{\gamma n}^{(i)}(E_{\mathrm{av}})$ represents the ith derivative of $\sigma_{\gamma n}(E_{\mathrm{av}})$. In order to determine $\sigma_{\gamma n}^{(i)}(E_{av})$, one must assume an energy dependence; hence an iteration procedure must be applied. The iteration procedure consists of the following four steps:

(1) We use the monochromatic cross section found from Eq. (6), $\sigma^{(0)}(E_{\mathrm{av}}) = \sigma_{\gamma n}^{\mathrm{mono}}(E_{\mathrm{av}})$, as our starting point and fit it with a Lorentzian function multiplied by a power law which dominates near S_n energies,

$$\sigma(E) = \sigma_c \left(\frac{E - S_n}{S_n}\right)^p \frac{1}{1 + \left(E^2 - E_R^2\right)^2/(E^2\Gamma^2)}, \quad (9)$$

where σ_c, p, E_R, and Γ are treated as free parameters [20].

(2) The fitted function $\sigma(E)$ is further divided into small regions of 300 keV, and each region is fitted by a third-order polynomial.

(3) The third-order polynomials are in turn used to calculate the derivatives $\sigma_{\gamma n}^{(i)}(E_{\mathrm{av}})$ in Eq. (8).

(4) Combining Eqs. (6) and (7), we get $\sigma(E_{\mathrm{av}})$ by

$$\sigma_{\gamma n}^{(1)}(E_{\mathrm{av}}) = \sigma_{\gamma n}^{\mathrm{mono}}(E_{\mathrm{av}}) - s_2(E_{\mathrm{av}}) - s_3(E_{\mathrm{av}}). \quad (10)$$

Here, we notice that the s_1 term cancels out.
The calculated photoneutron cross section $\sigma_{\gamma n}^{(1)}(E_{\mathrm{av}})$ is used for the next iteration; this procedure is followed until convergence is achieved.

We find that the series converges rather fast. Since the energy distribution of the beam is very sharp, the overall correction remains small, i.e., 0.5%–9%. As shown in Fig. 7, only cross sections located at the highest average energies are subject to a significant correction.

Our final photoneutron cross sections are compared in Figs. 8–14 with previous measurements, including the Saclay data [26]. Significant discrepancies are observed between our cross sections and those of Saclay for all Sm isotopes. Our experiment leads to cross sections lower by 20%–37%. Such an overestimate by the Saclay photodata was also reported in previous comparisons for ^{142}Nd with a renormalization by a factor of 0.86 [31], for ^{144}Sm by a factor of 0.80 [32], and for

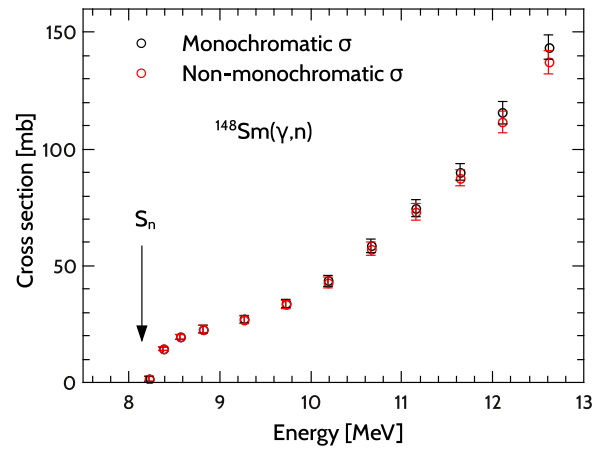

FIG. 7. (Color online) The monochromatic cross section and the nonmonochromatic cross section of ^{148}Sm. The arrow-indicated S_n gives the neutron threshold of this nucleus.

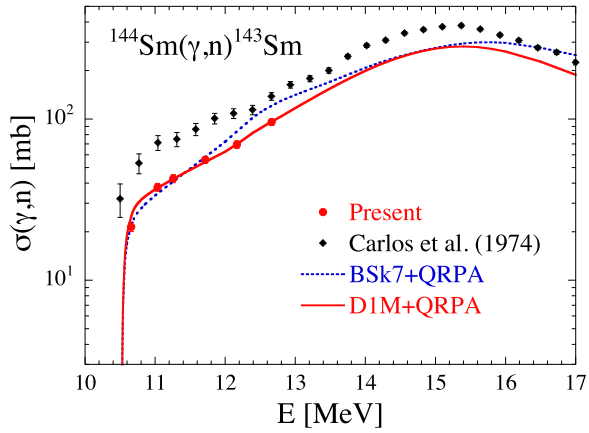

FIG. 8. (Color online) Comparison between the present photoneutron emission cross sections and previously measured ones [26] for ^{144}Sm. Also included are the predictions from Skyrme HFB+QRPA (based on the BSk7 interaction) [27] and axially deformed Gogny HFB+QRPA models (based on the D1M interaction) [28].

^{nat}Rb, ^{nat}Sr, ^{89}Y, ^{90}Zr, ^{93}Nb, ^{127}I, ^{197}Au, and ^{208}Pb by a factor of 0.80–0.93 [33].

IV. THEORETICAL ANALYSIS

The photoneutron cross-section data are now compared with theoretical calculations obtained with the TALYS nuclear reaction code [34,35] and two different models of the γSF, namely, the Skyrme Hartree-Fock-Bogoliubov (HFB) plus quasiparticle random phase approximation (QRPA) model [27] based on the BSk7 interaction and the axially symmetric deformed Gogny HFB plus QRPA model based on the D1M interaction [28,36–38]. Both models are based on the QRPA approach but make use of different interactions and approximations. The BSk7+QRPA model introduces some phenomenological corrections to take the damping of the collective motion as well as the deformation effects into account. In contrast, the D1M+QRPA model allows for a consistent description of axially symmetric deformations and includes phenomenologically the impact of multiparticle-multihole configuration as a function of their densities [28,37]. Both models have proven their capacity to reproduce experimental photoabsorption data relatively well.

As seen in Figs. 8–14, cross sections around the neutron threshold are rather well described by the D1M+QRPA model, provided a scaling within typically 10%–20% is applied to the strength function to reproduce the absolute experimental cross sections. The agreement around the neutron threshold is rather satisfactory and there is no reason to invoke the presence of extra low-lying strength from the present data, at least in the vicinity of the neutron threshold and as seen in some previous photodata [3,6,7,39]. In contrast, larger deviations are seen for the predictions obtained with the BSk7+QRPA strength where some extra strength is usually predicted around 11 MeV. Similar quantitative and qualitative results were obtained in the analysis of the photoneutron data for the Nd isotopes [9].

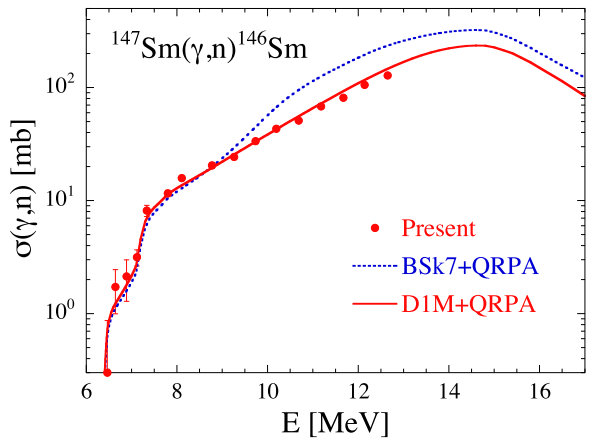

FIG. 9. (Color online) Same as Fig. 8 for ^{147}Sm.

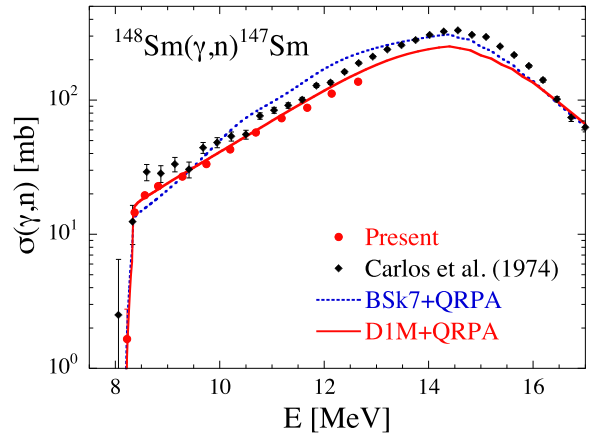

FIG. 10. (Color online) Same as Fig. 8 for ^{148}Sm.

V. RADIATIVE NEUTRON CAPTURE AND THE γSF METHOD

We now turn to the reverse radiative neutron capture channel. It should be kept in mind that the corresponding

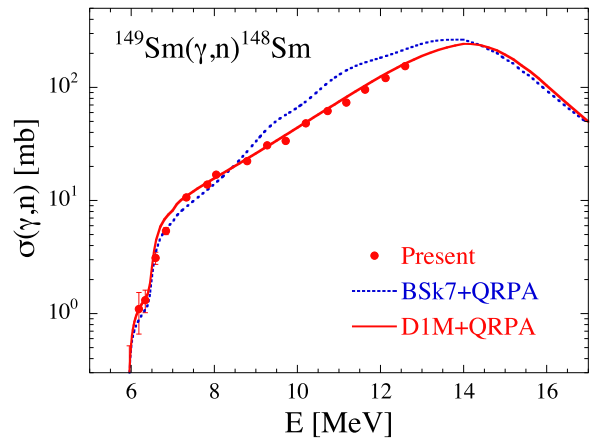

FIG. 11. (Color online) Same as Fig. 8 for ^{149}Sm.

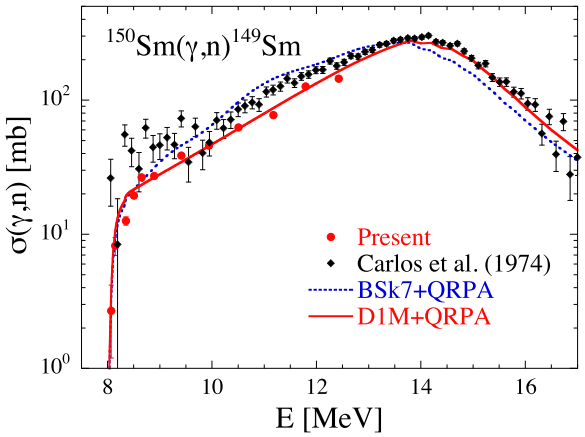

FIG. 12. (Color online) Same as Fig. 8 for ^{150}Sm.

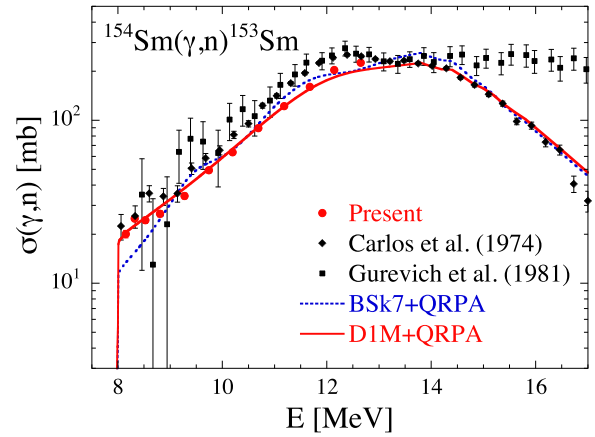

FIG. 14. (Color online) Same as Fig. 8 for ^{154}Sm. Experimental photoabsorption data from Ref. [30] are also included.

cross section for incident keV neutrons depends sensitively on the γSF, but in a rather lower energy range below the neutron threshold, typically around 6 MeV of γ-ray energy for the stable Sm isotopes, corresponding to the major contributing energy range in the folding of the γSF with the nuclear level density (NLD) [11,27]. The predicted tail of the strength function at low energies therefore plays a fundamental role.

On the basis of the Gogny HFB plus QRPA γ-ray strength [28], the reverse radiative neutron capture cross sections are now estimated with the TALYS reaction code [34,35] for the stable and experimentally known ^{147,148,149,150,151,152}Sm isotopes and compared with the experimental cross sections [26,29,30] in Fig. 15. Note that, in addition to the $E1$ contribution to the γSF, the smaller $M1$ and other higher multipolarities are included, following the prescriptions recommended in Refs. [34,35,54]. On top of the $E1$ strength function, the cross section calculation also depends on the adopted NLD. We have used here two versions of the HFB plus combinatorial model, namely, the original one from Ref. [55] and the latest version based on the temperature-dependent HFB model of Ref. [56]. Both of them are normalized to the experimental s-wave spacing D_0 values [54] whenever available.

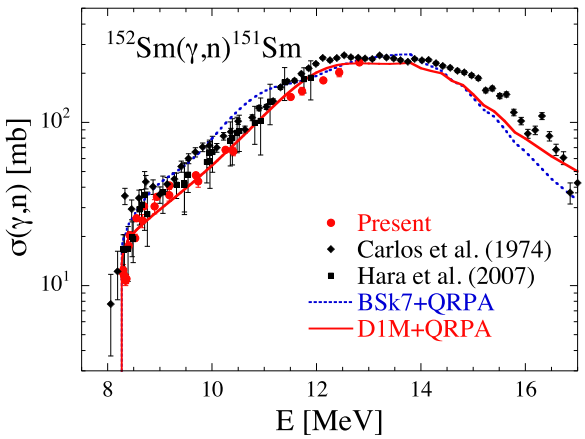

FIG. 13. (Color online) Same as Fig. 8 for ^{152}Sm. Experimental (γ,n) data from Ref. [29] are also included.

As can be seen in Fig. 15, the TALYS calculation agrees well with experimental data for all six Sm isotopes, which shows that, within the uncertainties affecting the experimental γSF and D_0 value, all γSF data are compatible with both the photoabsorption above the threshold and the radiative capture channels below the threshold. Experimental data exist for the ^{151}Sm$(n,\gamma)^{152}$Sm cross section and our predictions are in rather good agreement with the measurements. The corresponding TALYS Maxwellian-averaged cross section amounts, at the thermal energy of 30 keV, to 3200 ± 800 mb, where the uncertainty stems from the use of our two different NLD models [55,56]. This value is in agreement with the value of 3031 ± 68 mb found experimentally [13].

The γSF method can now be applied to the experimentally unknown neutron capture cross section of ^{153}Sm. The D1M+HFB $E1$ strength function positively tested on the photoneutron and radiative capture cross section is used. As far as the NLD is concerned, here also both versions of the HFB plus combinatorial models [55,56] are considered. No experimental information exists on the resonance spacing at the neutron binding energy for ^{154}Sm. The major uncertainty in the estimate of the neutron capture cross section therefore stems from the adopted NLD model. The final prediction is shown in Fig. 16. The Japanese JENDL-4.0 and American ENDF/B-VII.1 evaluations [57] are seen to be in relatively good agreement with our estimate, but the Russian ROSFOND-2010 evaluation gives rather lower cross sections below 10 keV. The resulting Maxwellian-averaged cross section of astrophysical interest amounts, at 30 keV, to 1285 ± 360 mb. Our estimate (and, consequently, also the ENDF/B-VII.1 and JENDL-4.0 ones) is found to be larger than the theoretical Maxwellian-averaged cross sections of 1095 ± 175 mb recommended in Ref. [58].

VI. CONCLUSIONS

Photoneutron cross sections were measured for all seven stable Sm isotopes near the neutron threshold with quasi-monochromatic laser-Compton scattering γ rays. Our photoneutron cross sections are found to be about 20%–37%

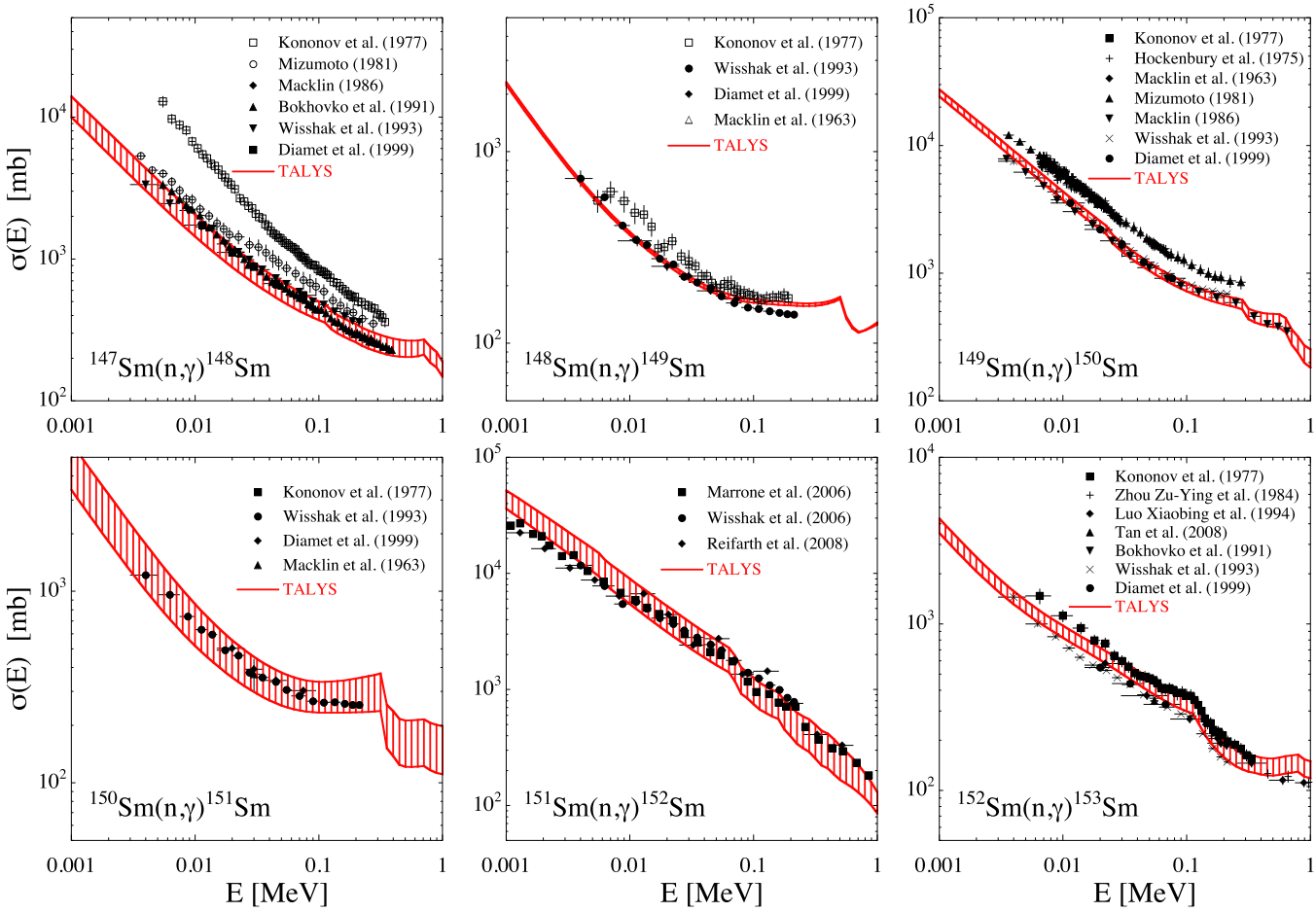

FIG. 15. (Color online) Comparison between the Sm measured radiative neutron capture cross sections [13,40–53] with a TALYS calculation making use of the D1M+QRPA calculation for the $E1$ strength. The hashed area corresponds to the sensitivity to the NLD.

lower relative to the 1974 measurements in Saclay [26]. The new data are analyzed with HFB+QRPA models of $E1$ γ-ray strength. The D1M+QRPA strength function is found to be able to reproduce fairly well the photodata in all the energy range above the neutron threshold and simultaneously

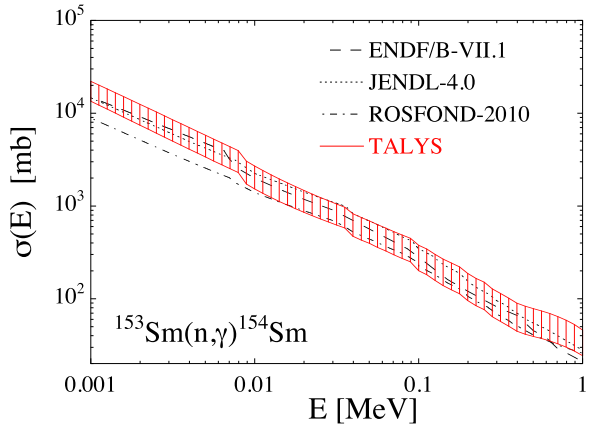

FIG. 16. (Color online) Prediction of the ^{153}Sm$(n,\gamma)^{154}$Sm cross section. The dotted, dashed, and dashed-dotted curves correspond to the Japanese JENDL-4.0, American ENDF/B-VII.1, and Russian ROSFOND-2010 evaluations [57], respectively.

the experimental neutron capture cross sections which are sensitive to the γSF below the threshold. A thorough analysis of the reverse (n,γ) cross sections is made including the radioactive nucleus ^{151}Sm with a half-life 90 yr and ^{153}Sm with a half-life 1.928 d through the γ-ray strength function method. While neutron capture measurements exist for ^{151}Sm, the new constraint on the ^{154}Sm $E1$ strength leads to a ^{153}Sm$(n,\gamma)^{154}$Sm cross section sensitively higher than the one predicted in previous works.

ACKNOWLEDGMENTS

This work was supported by the Japan Private School Promotion Foundation and by the JSPS-FNRS bilateral program. We are grateful to M. Igashira of the Tokyo Institute of Technology for making the ^{148,149,152,154}Sm samples available for the present experiment. We thank Florin Rotaru of the National Institute for Physics and Nuclear Engineering Horia Hulubei for initiating us into GEANT4 coding and for fruitful discussions. We acknowledge PRACE for awarding us access to the resource CURIE based in France at TGCC-CEA. D.M.F., I.G., and O.T. acknowledge financial support from the Extreme Light Infrastructure Nuclear Physics (ELI-NP) Phase I project, a project co-financed by the European Union through

the European Regional Development Fund. H.T.N. and T.R. acknowledge financial support from the Norwegian Research Council (NFR), Project No. 210007. S.G. acknowledges the financial support from the FNRS.

[1] F. Käppeler, R. Gallino, S. Bisterzo, and W. Aoki, Rev. Mod. Phys. **83**, 157 (2011).
[2] IAEA-TECDOC-985, IAEA, November 1997.
[3] H. Utsunomiya *et al.*, Phys. Rev. C **80**, 055806 (2009).
[4] H. Utsunomiya *et al.*, Phys. Rev. C **82**, 064610 (2010).
[5] D. M. Brink, Ph.D. thesis, Oxford University, 1955.
[6] H. Utsunomiya *et al.*, Phys. Rev. C **81**, 035801 (2010).
[7] H. Utsunomiya *et al.*, Phys. Rev. C **84**, 055805 (2011).
[8] H. Utsunomiya *et al.*, Phys. Rev. C **88**, 015805 (2013).
[9] H. T. Nyhus *et al.* (unpublished)
[10] M. Arnould and S. Goriely, Phys. Rep. **384**, 1 (2003).
[11] M. Arnould, S. Goriely, and K. Takahashi, Phys. Rep. **450**, 97 (2008).
[12] U. Abbondanno *et al.*, Phys. Rev. Lett. **93**, 161103 (2004).
[13] K. Wisshak, F. Voss, F. Käppeler, M. Krtička, S. Raman, A. Mengoni, and R. Gallino, Phys. Rev. C **73**, 015802 (2006).
[14] S. Amano *et al.*, Nucl. Instrum. Phys. Res. A **602**, 337 (2009).
[15] H. Utsunomiya *et al.*, IEEE Trans. Nucl. Sci. **61**, 1252 (2014).
[16] J. Allison *et al.*, IEEE Trans. Nucl. Sci. **53**, 270 (2006).
[17] S. Agostinelli *et al.*, Nucl. Instrum. Phys. Res. A **506**, 250 (2003).
[18] I. Gheorghe *et al.* (unpublished).
[19] B. L. Berman and S. C. Fultz, Rev. Mod. Phys. **47**, 713 (1975).
[20] O. Itoh *et al.*, J. Nucl. Sci. Technol. **48**, 834 (2011).
[21] T. Kondo *et al.*, Nucl. Instrum. Phys. Res. A **659**, 462 (2011).
[22] T. Kii *et al.*, in *Proceedings of the 12th Symposium on Accelerator Science and Technology*, edited by Yasushige Yano (The Institute of Physical and Chemical Research (RIKEN), Wako, Japan, 1999), pp. 484–485.
[23] H. Toyokawa, T. Kii, H. Ohgaki, T. Shima, T. Baba, and Y. Nagai, IEEE Trans. Nucl. Sci. **47**, 1954 (2000).
[24] NIST Physical Measurement Laboratory, http://physics.nist.gov/PhysRefData/XrayMassCoef/tab3.html.
[25] H. Utsunomiya *et al.*, Phys. Rev. C **74**, 025806 (2006).
[26] P. Carlos, H. Beil, R. Bergere, A. Lepretre, A. Deminiac, and A. Veyssiere, Nucl. Phys. A **225**, 171 (1974).
[27] S. Goriely, E. Khan, and M. Samyn, Nucl. Phys. A **739**, 331 (2004).
[28] M. Martini, S. Hilaire, S. Goriely, A. J. Koning, and S. Péru, Nucl. Data Sheets **118**, 273 (2014).
[29] K. Y. Hara *et al.*, J. Nucl. Sci. Technol. **44**, 938 (2007).
[30] G. M. Gurevich, L. E. Lazareva, V. M. Mazur, S. Yu. Merkulov, G. V. Solodukhov, and V. A. Tyutin, Nucl. Phys. A **351**, 257 (1981).
[31] C. T. Angell *et al.*, Phys. Rev. C **86**, 051302(R) (2012).
[32] C. Nair *et al.*, Phys. Rev. C **81**, 055806 (2010).
[33] B. L. Berman, R. E. Pywell, S. S. Dietrich, M. N. Thompson, K. G. McNeill, and J. W. Jury, Phys. Rev. C **36**, 1286 (1987).
[34] A. J. Koning, S. Hilaire, and M. Duijvestijn, in *Nuclear Data for Science and Technology*, edited by O. Bersillon, F. Gunsing, E. Bauge, R. Jacqmin, and S. Leray (EDP Sciences, Les Ulis, France, 2008), p. 211.
[35] A. J. Koning and D. Rochman, Nucl. Data Sheets **113**, 2841 (2012).
[36] S. Péru and H. Goutte, Phys. Rev. C **77**, 044313 (2008).
[37] S. Péru and M. Martini, Eur. Phys. J. A **50**, 88 (2014).
[38] S. Goriely, S. Hilaire, M. Girod, and S. Péru, Phys. Rev. Lett. **102**, 242501 (2009).
[39] T. Kondo *et al.*, Phys. Rev. C **86**, 014316 (2012).
[40] V. N. Kononov, B. D. Jurlov, E. D. Poletaev, V. M. Timokhov, and G. N. Manturov, Yad. Konstanty **22**, 29 (1977).
[41] R. L. Macklin, N. W. Hill, J. A. Harvey, and G. L. Tweed, Phys. Rev. C **48**, 1120 (1993).
[42] M. Mizumoto, Nucl. Phys. A **357**, 90 (1981).
[43] R. Macklin, EXFOR database, https://www-nds.iaea.org/exfor.
[44] M. V. Bokhovko, V. N. Kononov, N. S. Rabotnov, A. A. Voevodskiy, G. N. Manturov, and V. M. Timokhov, Fiz.-Energ Institut, Obninsk, Report No. 2168, 1991.
[45] K. Wisshak, K. Guber, F. Voss, F. Käppeler, and G. Reffo, Phys. Rev. C **48**, 1401 (1993).
[46] B. Diamet, M. Igashira, M. Mizumachi, S. Mizuno, J.-I. Hori, K. Masuda, and T. Ohsaki, J. Nucl. Sci. Technol. **36**, 865 (1999).
[47] R. L. Macklin, J. H. Gibbons, and T. Inada, Nature (London) **197**, 369 (1963).
[48] R. W. Hockenbury, W. R. Koste, and R. A. Shaw, Bull. Am. Phys. Soc. **20**, 560 (1975).
[49] S. Marrone *et al.*, Phys. Rev. C **73**, 034604 (2006).
[50] R. Reifarth, T. A. Bredeweg, A. Couture, E.-I. Esch, and U. Greife, in *10th Symposium on Nuclei in the Cosmos*, edited by H. Schatz, S. Austin, T. Beers, Ed Brown, B. Lynch, and R. Zegers (SISSA, Trieste, Italy, 2008), p. 84.
[51] Z.-Y. Zhou, Y. Chen, S.-S. Jiang, and D.-X. Luo, Chin. J. Nucl. Phys. **6**, 174 (1984).
[52] X. Luo, Y. Xia, Z. Yang, and M. Liu, Chin. J. Nucl. Phys. **16**, 275 (1994).
[53] V. H. Tan, T. T. Anh, N. C. Hai, P. N. Son, and T. Fukahori, JAEA Conf. Proc. **006**, 40 (2008).
[54] R. Capote *et al.*, Nucl. Data Sheets **110**, 3107 (2009).
[55] S. Goriely, S. Hilaire, and A. J. Koning, Phys. Rev. C **78**, 064307 (2008).
[56] S. Hilaire, M. Girod, S. Goriely, and A. J. Koning, Phys. Rev. C **86**, 064317 (2012).
[57] Evaluated Nuclear Data Files, 2011, http://www-nds.iaea.or.at/exfor.htm.
[58] Z. Y. Bao, H. Beer, F. Käppeler, F. Voss, K. Wisshak, and T. Rauscher, At. Data Nucl. Data Tables **76**, 70 (2000).